IOP Publishing Physics in Medicine and Biology

Phys. Med. Biol. **52** (2007) 4615–4632 doi:10.1088/0031-9155/52/15/017

Novel approach to stationary transmission scanning using Compton scattered radiation

M K Nguyen[1], T T Truong[2], J L Delarbre[1], Ch Roux[3,4] and H Zaidi[5]

[1] Laboratoire Equipes de Traitement des Images et du Signal (CNRS UMR 8051/ENSEA/Université de Cergy-Pontoise), 6, avenue du Ponceau, 95014 Cergy-Pontoise, France
[2] Laboratoire de Physique Théorique et Modélisation (CNRS UMR 8089), Université de Cergy-Pontoise, 95031 Cergy-Pontoise Cedex, France
[3] GET-ENST Bretagne, Laboratoire de Traitement de l'Information Médicale (LaTIM), Brest, F-29200, France
[4] INSERM, U650, Brest, F-29200, France
[5] Geneva University Hospital, Division of Nuclear Medicine, CH-1211 Geneva 4, Switzerland

E-mail: nguyen@ensea.fr, tuong.truong@u-cergy.fr and habib.zaidi@hcuge.ch

Received 1 March 2007, in final form 4 June 2007
Published 10 July 2007
Online at stacks.iop.org/PMB/52/4615

Abstract

Transmission scanning-based estimation of the attenuation map plays a crucial role in quantitative radionuclide imaging. X-ray computed tomography (CT) reconstructs directly the attenuation coefficients map from data transmitted through the object. This paper proposes an alternative route for reconstructing the object attenuation map by exploiting Compton scatter of transmitted radiation from an externally placed radionuclide source. In contrast to conventional procedures, data acquisition is realized as a series of images parameterized by the Compton scattering angle and registered on a stationary gamma camera operating without spatial displacement. Numerical simulation results using realistic voxel-based phantoms are presented to illustrate the efficiency of this new transmission scanning approach for attenuation map reconstruction. The encouraging results presented in this paper may suggest the possibility of proposing a new concept for emission/transmission imaging using scattered radiation, which has many advantages compared to conventional technologies.

1. Introduction

Quantitative radionuclide imaging faces a double challenge as it must deal simultaneously with two physical degrading factors: photon attenuation in the patient's body (Zaidi and Hasegawa 2003) and the detection of Compton scattered photons (Zaidi and Koral 2004). In nuclear imaging, Compton scatter is the companion of photon attenuation. That is, a large fraction of

the photons that are attenuated instantly fall into the category of a potential scatter-corrupting photon. A photoelectric absorption contributes only to attenuation, but a Compton scatter interaction increases attenuation and also sets up a potential scatter corruption. Uncorrected data are therefore of little relevance for medical diagnosis and radiation therapy planning, since clinically relevant features may not be suitably exposed to the scrutiny of physicians. This explains why attenuation correction in nuclear imaging has been always a domain of intense research interest (Zaidi and Hasegawa 2003).

In x-ray computed tomography (CT), which delivers anatomical information, the object under study, e.g. the human body, is characterized by its attenuation properties. The working principle of CT is based on the Radon transform of the attenuation map, which was introduced by J Radon in his seminal paper of 1917 (Radon 1917). However, in radionuclide tomographic imaging (SPECT or PET), the aim is to reconstruct the distribution of a radiotracer to obtain related functional or physiological information. In this case, attenuation intervenes as an impairing factor. Thus a substantial number of algorithms have been designed to cope with the attenuation effect (Barrett 1981, Gullberg *et al* 1985, King *et al* 1996, Zaidi and Hasegawa 2003). In radionuclide imaging, the image formation process in the presence of a known nonuniform attenuation map is described by the attenuated x-ray transform of the activity distribution. Thus, the proper approach to solving the attenuation problem consists in finding the analytic inversion of this transform. This turned out to be an open mathematical problem for many years, and has been solved only recently (Novikov 2002). Determining the attenuation map of an object is therefore an indispensable task to perform image reconstruction in nuclear imaging.

In this work, we deal mainly with attenuation due to Compton scattering owing to the fact that for single-photon emitting radiotracers used for nuclear imaging, absorption by photoelectric effect is negligible (Zaidi and Hasegawa 2003). The use of scattered radiation has been advocated long ago (Cesareo *et al* 1992) as a means to reconstruct the electron density map n_e, which is in turn is related to the local attenuation coefficient of the medium (Clarke *et al* 1976, Hussein 1989). This idea has been implemented in the so-called 'Compton tomography' concept, in which gamma rays from a fixed point source illuminate an object and scattered radiation is detected by a movable collimated pixel detector (Battista and Bronskill 1981, Holt *et al* 1984, Norton 1994). Unfortunately this procedure introduces a new attenuated Radon transform on tori, for which an inversion formula is not available (except in two dimensions). Thus up to now, the way scattered radiation could be exploited to determine attenuation in a satisfactory way remained an open problem.

Recently, an elegant approach was proposed to exploit Compton radiation scattering in gamma-ray emission imaging (Nguyen and Truong 2002a, 2002b, Nguyen *et al* 2004, Truong *et al* 2007). Instead of considering scatter as an unwanted factor which decreases image quality and quantitative accuracy, it was proposed to exploit it to establish a novel imaging principle based on measurement of Compton scattered radiation. Image formation is now modeled by neglecting attenuation effects using the so-called compounded conical Radon transform (CCRT) (Nguyen and Truong 2002a). This transform is shown to be invertible and uses, for its inversion, data collected at different scattering angles, instead of the spatial rotation angle of the camera. The feasibility of three-dimensional (3D) object reconstruction from its scattered radiation is thereby established. An important by-product of this new imaging principle turns out to be a novel approach to performing transmission scanning in order to estimate the attenuation map, which is the main topic addressed in this paper.

We present the working principle of this new concept for determining the electron density n_e from scattered radiation. It consists in illuminating the object by a point source of known intensity and location in space and detecting scattered radiation by a standard stationary

collimated gamma camera (in a fixed position). This situation is in fact a particular case of scattered radiation imaging of an extended radiating object as described in Nguyen and Truong (2002a). But now the unknown is not the source activity distribution but the electron density n_e. An inversion formula therefore exists giving n_e in terms of the photon flux density measured on the detector. As n_e and the linear attenuation coefficient are interrelated, we show that the use of this inversion formula together with an appropriately constructed correction algorithm leads to a very accurate estimation of the object attenuation map. The analysis of the numerical behavior of the correction procedure is realized. Simulations on realistic voxel-based phantoms are presented followed by a discussion of the reconstruction results. Finally, perspectives for dual-modality emission/transmission imaging based only on scattered radiation are discussed. Note that a considerable number of dual-modality imaging technologies have been developed during the last decade combining SPECT (or PET) imaging with x-ray CT (Keidar *et al* 2003) or through transmissionless derivation of the attenuation map (Gourion *et al* 2002). However, none of them use scattered radiation directly for imaging. The work presented here focuses on an alternative technique for reconstructing the object attenuation map by exploiting Compton scattered radiation from an external radionuclide transmission source.

2. Materials and methods

2.1. Novel reconstruction method of electron density using Compton scattered radiation

In this section we describe a novel method to determine the electron density of an object, which subsequently leads to determination of its attenuation map.

To present the working principles, let us recall the principle of emission imaging using Compton scattered radiation. An object (e.g. human organ) in which a radiotracer (e.g. ^{99m}Tc) is injected emits gamma photons of energy $E_0 = 140$ keV. In conventional SPECT imaging, a collimated gamma camera collects the emitted photons along a given direction and produces a projection. Using a set of projections from a sufficient number of angular directions, the object can be reconstructed in three dimensions revealing its inner functional state. However, photon scattering inside the medium will blur the recorded data and affect strongly the quality of the resulting reconstructions.

On the other hand, if one sets the gamma camera to operate in stationary mode (from a fixed position) to record scattered photons (instead of primary photons) of lower energies E (90 keV $< E <$ 140 keV), then a series of images labeled by E can be generated. If one considers that most of these photons will undergo single Compton scattering with electrons inside the object (since higher order scattered photons have much lower probability of being detected in this window, as reported in many Monte Carlo simulation studies (Zaidi 1999, Kojima *et al* 1999, Zaidi and Koral 2004)), then the recorded data are directly related to the electronic distribution n_e. As shown in Nguyen and Truong (2002a), the photon flux density measured on the gamma camera is expressed by the CCRT of the object activity density. Object reconstruction is consequently described by the inversion of the CCRT. This has been done in Nguyen and Truong (2002b) at constant electronic density and without attenuating effects.

In general, to account correctly for attenuation effects, the image formation should be modeled by the attenuated compounded conical Radon transform (or a-CCRT), in which attenuation factors are introduced along the photon paths. The a-CCRT formulation is similar to the well-known attenuated x-ray transform. However, its inverse has not been found yet, even if the attenuation map is known beforehand. In an ideal situation, one should be able to determine at the same time electron density (or attenuation map) and activity distribution from

one set of measurements. Since this is not the case, we shall proceed by approximations as often done to tackle difficult problems (Zeng *et al* 2002). We begin by considering the CCRT formulation of the image formation process in the presence of nonuniform electron density n_e. This time we regard n_e as unknown and assume the activity distribution to be given. In fact, the transmission scanning system simply consists of a calibrated point source positioned at a known site. The photon flux density measured by the camera gives a first direct estimate of n_e. We therefore propose an iterative method, based on the properties of the CCRT, to construct the object attenuation map. This method presents two main advantages:

– the attenuation map constructed in this way is photon energy dependent;

– the data acquisition procedure, which consists in collecting series of images at various scattering angles, is performed without having to move the detector.

As this new imaging concept uses scattered radiation, it requires high performance detector systems with excellent energy resolution. Thus, this concept is not meant to work on standard Anger cameras but might be applicable on new generation solid-state systems such as cadmium zinc telluride (CZT) detector arrays (Kim *et al* 2006, Gagnon *et al* 2001). Possible angular uncertainties related to finite detector energy resolution may be treated as in the case of Compton cameras (Hirasawa and Tomitani 2004, Mihailescu *et al* 2007). It is recognized that ignoring higher order scattering owing to the complexity of the model is one major limitation of this work and will be targeted for further research. In subsection 2.1.1, we describe first the working principles of our method and then in subsection 2.2 the corresponding iterative attenuation correction algorithm.

2.1.1. Electron density computation. In this subsection, we establish the relation giving the electron density in terms of the measured scattered photon flux density and the point source intensity.

Let **S** be the location of a point source of intensity f_0, which is the number of photons emitted uniformly per unit time around the 4π solid angle (figure 1). The number of photons per unit time emitted along a direction **n** in a solid angle $\mathrm{d}\Omega_{\mathbf{n}}$ is

$$\frac{f_0}{4\pi}\,\mathrm{d}\Omega_{\mathbf{n}}. \tag{1}$$

From this emitting site **S**, there will be an incoming flux density on a scattering site **M** located at a distance SM (with $SM = |\overrightarrow{SM}|$) from **S** equal to

$$\frac{f_0}{4\pi SM^2}. \tag{2}$$

At this site **M**, there are $n_e(\mathbf{M})\,\mathrm{d}\mathbf{M}$ electrons in a volume $\mathrm{d}\mathbf{M}$ around **M**. The number of scattered photons per unit area arriving at the detection site **D** on the gamma camera under a scattering angle θ is

$$\mathrm{d}g(\mathbf{D},\theta) = \frac{f_0}{4\pi SM^2} n_e(\mathbf{M})\,\mathrm{d}\mathbf{M}\frac{\mathrm{d}\sigma^C}{\mathrm{d}\Omega}\frac{1}{MD^2}\mathcal{A}_\mu(SM, MD), \tag{3}$$

where $\frac{\mathrm{d}\sigma^C}{\mathrm{d}\Omega}$ is the Compton differential cross section given by the Klein–Nishina formula (Barrett 1981). Since the product of the incoming flux density by the number of scatterers and by the Compton scattering cross section yields the number of particles scattered in the solid angle in the direction of angle θ, we must introduce the factor $1/MD^2$ (the square of the distance from site **M** to site **D**), to get the flux density arriving at detection site **D**.

$\mathcal{A}_\mu(SM, MD)$ represents the total attenuation factor from emission to detection

$$\mathcal{A}_\mu(SM, MD) = \exp\left(-\int_{SM}\mu(\mathbf{r}, E_0)\delta(SM)\,\mathrm{d}\mathbf{r} - \int_{MD}\mu(\mathbf{r}, E)\delta(MD)\,\mathrm{d}\mathbf{r}\right), \tag{4}$$

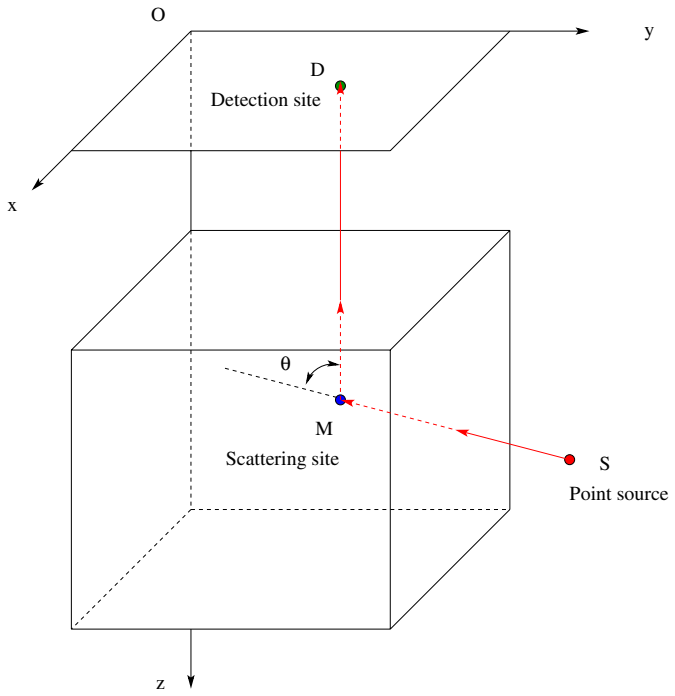

Figure 1. Geometric parameters of photon scattering in a medium resulting from point source transmission scanning.

where $\mu(\mathbf{r}, E)$ is the linear attenuation coefficient at site $\mathbf{r}$ and energy E which can be expressed in terms of $\sigma_E(\mathbf{r})$, the Compton cross section at energy E of material at site $\mathbf{r}$, as

$$\mu(\mathbf{r}, E) = \sigma_E(\mathbf{r}) n_e(\mathbf{r}). \tag{5}$$

The delta distributions restrict the integration to lines SM and MD in equation (4).

The flux density at the detector per unit volume is a nonlinear functional of n_e given by

$$\frac{\mathrm{d}g(\mathbf{D}, \theta)}{\mathrm{d}\mathbf{M}} = \frac{f_0}{4\pi} \frac{1}{SM^2} n_e(\mathbf{M}) \frac{\mathrm{d}\sigma^C}{\mathrm{d}\Omega} \frac{1}{MD^2} \mathcal{A}_\mu(SM, MD). \tag{6}$$

Therefore obtaining n_e directly from the measurement of $\mathrm{d}g(\mathbf{D}, \theta)/\mathrm{d}\mathbf{M}$ would not be possible. This is why an alternative strategy is proposed. The idea is to start first with a linearized form of equation (6), which is quite natural

$$\frac{\mathrm{d}g(\mathbf{D}, \theta)}{\mathrm{d}\mathbf{M}} = \widetilde{g}(\mathbf{D}, \theta) = \frac{f_0}{4\pi} \frac{1}{SM^2} n_e(\mathbf{M}) \frac{\mathrm{d}\sigma^C}{\mathrm{d}\Omega} \frac{1}{MD^2}, \tag{7}$$

which precisely amounts to neglecting the nonlinear factor $\mathcal{A}_\mu(SM, MD)$ and construct an efficient algorithm based on equation (7). This is done in the next subsection.

2.2. Iterative attenuation correction algorithm (IAC) using scattered radiation

Because of the presence of the collimator, site $\mathbf{M}$ is just situated on a line parallel to the collimator axis at site $\mathbf{D}$. So in an appropriately chosen coordinate system, we would have for

a given point source located at $\mathbf{S} = (x_S, y_S, z_S)$, $(x_M = x_D, y_M = y_D)$ and $\mathbf{D} = (x_D, y_D, 0)$. Consequently,

$$\widetilde{g}(\mathbf{D}, \theta) = n_e(x_M, y_M, z_M)\frac{f_0}{4\pi}\frac{\mathrm{d}\sigma^C}{\mathrm{d}\Omega}\frac{1}{(x_M - x_S)^2 + (y_M - y_S)^2 + (z_M - z_S)^2}\frac{1}{z_M^2}, \tag{8}$$

with

$$z_M = z_S - \cot\theta\sqrt{(x_M - x_S)^2 + (y_M - y_S)^2},$$

or alternatively

$$\widetilde{g}(\mathbf{D}, \theta) = n_e(x_D, y_D, z_S - \cot\theta\sqrt{(x_D - x_S)^2 + (y_M - y_S)^2})$$

$$\frac{f_0}{4\pi}\frac{\mathrm{d}\sigma^C}{\mathrm{d}\Omega}\frac{\sin^2\theta}{(x_M - x_S)^2 + (y_M - y_S)^2}\frac{1}{(z_S - \cot\theta\sqrt{(x_M - x_S)^2 + (y_M - y_S)^2})^2}. \tag{9}$$

Therefore one may rewrite equation (9) to extract the electronic density as

$$n_e(x_M, y_M, z_M) = \widetilde{g}(x_M, y_M, \theta)\frac{4\pi}{f_0\left(\frac{\mathrm{d}\sigma^C}{\mathrm{d}\Omega}\right)}z_M^2((x_M - x_S)^2 + (y_M - y_S)^2 + (z_M - z_S)^2). \tag{10}$$

In fact, this is only a first estimate of n_e. If the attenuation factor is taken into account, equation (10) would have the form

$$\begin{aligned} n_e(x_M, y_M, z_M) &= \widetilde{g}(x_M, y_M, \theta)\frac{4\pi}{f_0\left(\frac{\mathrm{d}\sigma^C}{\mathrm{d}\Omega}\right)}\frac{1}{\mathcal{A}_\mu(SM, MD)} \\ &\quad z_M^2((x_M - x_S)^2 + (y_M - y_S)^2 + (z_M - z_S)^2). \end{aligned} \tag{11}$$

These considerations suggest the formulation of an attenuation correction algorithm as described in the following steps. Since μ is unknown, $\mathcal{A}_\mu(SM, MD)$ is also unknown. We aim to obtain the best possible estimate of n_e using equation (5) with what is available at hand, i.e., equation (10).

Thus starting from actually collected data on the detector $\widetilde{g}(\mathbf{D}, \theta)$, identified as the zeroth step data $\widetilde{g}^0(\mathbf{D}, \theta)$, the use of equation (10) would yield a first estimate of the electronic density which shall be called $n_e(0)$. From now on to simplify notation we shall drop the spatial dependence of $n_e(\mathbf{r})$ as stated in equation (5) and denote the jth step value of n_e by $n_e(j)$. We obtain a first estimate of μ using equation (5), which shall be denoted μ^0 and then compute the attenuation factor $\mathcal{A}_{\mu^0}$ to obtain the first corrected estimate as

$$\frac{\widetilde{g}^0(\mathbf{D}, \theta)}{\mathcal{A}_{\mu^0}} = \widetilde{g}^1(\mathbf{D}, \theta), \tag{12}$$

where the attenuation effect has been removed in this first step. Thus the correction is aimed at obtaining collected data in the absence of attenuation.

We can repeat the procedure starting from $\widetilde{g}^1(\mathbf{D}, \theta)$, instead of $\widetilde{g}^0(\mathbf{D}, \theta)$, reconstruct $n_e(1)$ using equation (10), compute μ^1 (using equation (5)) and $\mathcal{A}_{\mu^1}$ (using equation (4)) and end up with $\widetilde{g}^2(\mathbf{D}, \theta)$. The iterative process will be stopped whenever the mean relative quadratic error $(MRQE)_{n_e}$ between two consecutive values $n_e(j-1)$ and $n_e(j)$, for $j = 1, 2, \ldots,$ is less than a given threshold (1% for example). This process is called the iterative attenuation correction (IAC) algorithm and is summarized in figure 2.

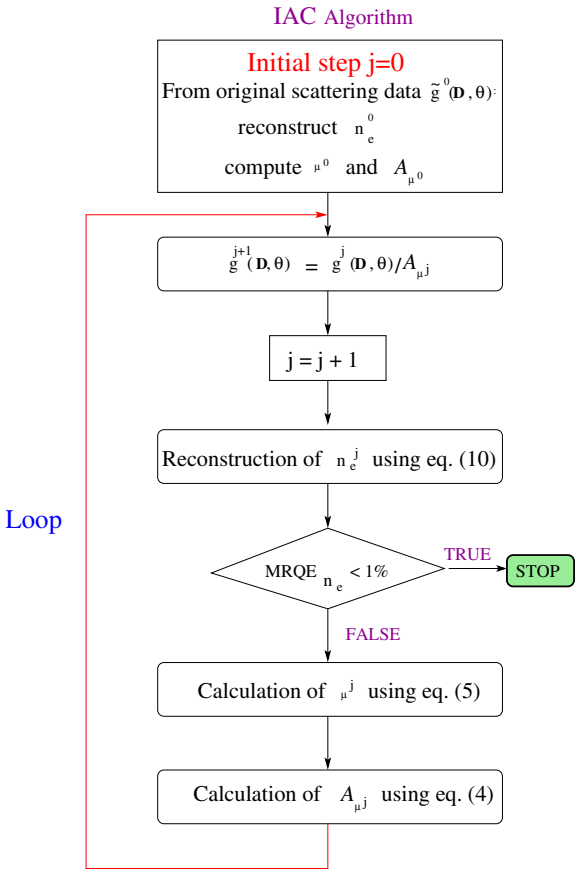

Figure 2. Flowchart of the iterative attenuation correction (IAC) algorithm.

2.3. Practical considerations for the implementation of the IAC algorithm

In the human body, one may simplify things by assuming that the only materials found are soft tissues and bones (lungs are also soft tissues). However, their average atomic number Z is not directly accessible. It is usually admitted that soft tissue is structurally close to water and its electronic density may vary but will never come close to that of bone or air (e.g. lungs). Similar considerations are valid for bone or lung tissues. So an estimated value of $n_e(\mathbf{r})$ allows us to determine what type of material is met at the studied site. Using *a priori* knowledge about existing materials at a particular point of interest, we can estimate its average atomic number Z and consequently assess its scattering cross section $\sigma_{E,m}(\mathbf{r})$ for a material m and compute its attenuation coefficient. The IAC algorithm so set up should provide the best possible reconstruction of the medium electron density.

On each line perpendicular to the detector equipped with a parallel hole collimator, the location of the scattering site could be determined by the photon energy for given a given point source position. Geometrically, for a gamma ray emanating from a point source **S**, the scattering angle fixes only the scattering site **M** on the line perpendicular to the detector at **D**, because of collimated detection. Better angular accuracy implies better geometrical accuracy. If the radiating point source is placed on the opposite side of the detector after the object, the

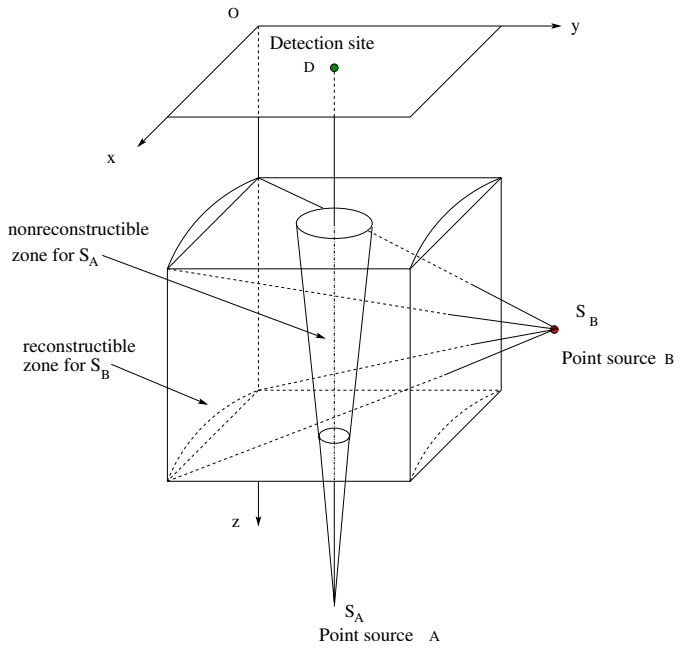

Figure 3. Source *A* does not allow correct reconstruction inside the cone whereas source *B* allows a correct reconstruction of the entire object.

majority of interactions will be small angle scattering. Thus scattering sites will be located inside a thin cone, as shown in figure 3. Collected scatter data are then concentrated and not usable. This is the reason why it is more appropriate to place the source on the side of the object as shown in figure 3 (point source *B*). In this way, for the same energy resolution of the detector, more scattering sites will contribute to the image.

2.4. Convergence behavior of the IAC algorithm

2.4.1. General observations. In this section we present convergence arguments for the practical implementation of the IAC algorithm. We first make some general observations on the nature of errors one may encounter. A detailed mathematical discussion of the convergence of the process is beyond the scope of this paper and will be the subject of future research. Instead, we will propose a simplified but realistic model to show how convergence can be reached for a given site of the object. The results will then be applied to the totality of its sites. This of course leads to additional corrections to be carried out whenever convergence is poor or non-existing in order to achieve a realistic reconstruction at the end.

Equations (10) and (5) are used cyclically to estimate electronic density and photon flux density at a site of the detector. Equation (6) shows that global loss of photons depends on the product $n_e \mathcal{A}(d)$, where d is the mean length of the photon path. But attenuation itself is also directly dependent on electronic density. So if n_e is overestimated, the excess of scattered photons at the scattering site may be compensated by a stronger attenuation along the photon path. Thus, there may be more than one object giving rise to the same recorded data.

The IAC algorithm realizes a stepwise estimation of n_e and a stepwise correction to the number of photons on a detection pixel. The jth step estimation of n_e should in principle

produce a more accurate estimation of attenuation than the preceding step and in turn should give a better estimate of n_e. However, at this stage, the estimate may be larger or smaller than its expected nominal value.

Let us assume that n_e is overestimated at this jth step. The attenuation will be also too high, which means a lower value of $\mathcal{A}$ in equation (13). Three possibilities may arise:

(i) Roughly one may say that the product $n_e\mathcal{A}$ has correct values but with wrong values of n_e and $\mathcal{A}$. The algorithm yields a wrong estimate for n_e.
(ii) The product $n_e\mathcal{A}$ is underestimated, the values of n_e are at first too large but will decrease and will then tend toward the correct value at the end.
(iii) The product $n_e\mathcal{A}$ is too large. In the next step, n_e would be further overestimated. The error increases with the iterations and leads to a wrong result.

An analogous reasoning can be made when n_e is at first underestimated.

Thus the question which should be raised here is how a correct value of n_e can be obtained from the fluctuating number of detected photons at a camera pixel at each step of the algorithm. Attenuation along a photon *travel* path is mainly due to scattering and reduces the number of photons reaching the detection pixel. As we are dealing with the human body, we may assume, for simplicity, that the electronic density remains constant over large areas representing lungs, muscles or bones and argue with a simplified version of photon detection given by equation (11). With this hypothesis, $\widetilde{g}$, the number of photons at a detection pixel per unit time and unit pixel area at some energy E, can be expressed as

$$\widetilde{g} = n_e\mathcal{A}(d)C \tag{13}$$

where n_e is the electronic density of the medium, $\mathcal{A}(d)$, the total attenuation along the photon path from emission to detection over a distance d and C a constant representing other effects, not relevant to this discussion.

2.4.2. Recursion relation for the estimation of n_e. With the previous assumptions we show now that the study of the convergence of the estimates of n_e is equivalent to that of a simple recursion relation which depends on one parameter.

Recall that $n_e(j)$ is the estimated value of n_e at step j of the process. According to our prescription, this means that we have a sequence of estimated $\mathcal{A}_j(d)$ attenuation factors, labeled by j, coming from the previous step of the form

$$\mathcal{A}_j(d) = \mathrm{e}^{-\sigma n_e(j-1)d}. \tag{14}$$

Since one must have for all $j = 1, 2, \ldots$ steps the same actual number of detected photons, we should have

$$\widetilde{g} = n_e\mathcal{A}(d)C = n_e(j)\mathcal{A}_j(d)C. \tag{15}$$

From this relation, we extract

$$n_e(j) = n_e\frac{\mathcal{A}(d)}{\mathcal{A}_j(d)}. \tag{16}$$

Now suppose we represent the jth estimate of n_e as

$$n_e(j) = \alpha_j n_e, \tag{17}$$

where α_j is a positive number. Plugging this form into equation (16) yields a recursion relation for the α_j:

$$\alpha_j = \mathcal{A}^{(1-\alpha_{j-1})}(d), \tag{18}$$

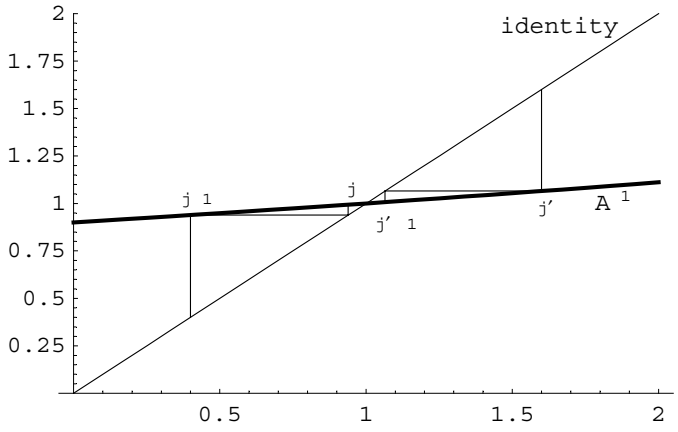

Figure 4. The α_j and α'_j sequences converge towards 1 for starting values smaller and bigger than 1 (here $\mathcal{A} = 0.9$).

with the initial condition $\alpha_0 = \mathcal{A}$. The question of convergence of the algorithm may be transferred to the convergence of the sequence α_j for different values of the parameter $\mathcal{A}$.

Equation (18) is a recursion relation for the sequence α_j. In general, the convergence of a sequence x_j, defined by the recursion relation $x_j = f(x_{j-1})$, towards a fixed point x^* is guaranteed if $|f'| < 1$ in the neighborhood of x^*. We will analyze this convergence in the next paragraphs with the observation that $\mathcal{A}(d)$, being an attenuation factor, has a value lower than 1.

2.5. Convergence of the IAC algorithm for various scattering sites of the object

As pointed out in the last subsection, the relevant parameter of the recursion relation is the attenuation factor $\mathcal{A}(d)$, which is a function of d, the distance traveled by the photon. Thus we discuss the convergence of the IAC algorithm at each site of the object.

2.5.1. Scattering sites near the point source. If the distance traveled by scattered photons (near the external source) in the medium is rather short, attenuation is low ($\mathcal{A} \simeq 1$). As an example, for $\mathcal{A} = 0.9$, figure 4 shows a good convergence of α_j towards 1, with α_j taking values above or below 1.

Thus the electronic density at points near the external source is correctly estimated and attenuation correction is stable, as we can see in numerical simulations.

2.5.2. Scattering sites far from the point source. Now if the distance covered by scattered photons in the medium is rather long, attenuation is high and $\mathcal{A}(d)$ is low. For $\mathcal{A}(d) = 0.15$, figure 5 shows two fixed points for the α_j sequence, one of them ($\alpha_j = 1$) is repulsive, so that the more we iterate the worst is the estimate of n_e. With a higher starting value, $n_e(j)$ will grow indefinitely. But with a lower starting value, α_n will converge to another fixed point. $n_e(j)$ will never tend to infinity since we know that $\alpha_0 = \mathcal{A}$, which is always lower than the second and non-repulsive fixed point.

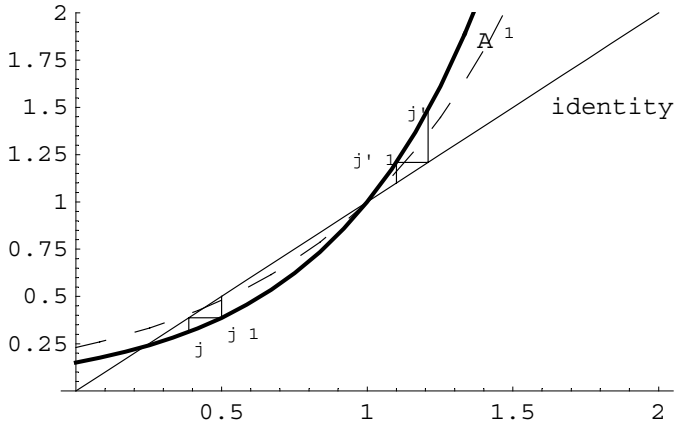

Figure 5. The α_j sequence converges towards a non-suitable solution for α_j value which is smaller than 1 and diverges for values higher than 1 ($\mathcal{A} = 0.15$). As an example, we show with the dashed line the graph of $\mathcal{A}^{1-\alpha}$ for $\mathcal{A} = 0.23$.

The results are not good for electronic density estimation using this attenuation correction scheme for scattering points far away from the external lighting source. n_e^n converges towards a lower value of n_e. This calls for the need of an additional correction.

2.5.3. Critical attenuation value. Two different convergence behaviors arise in the practical implementation of the IAC algorithm depending on the value of the parameter $\mathcal{A}(d)$. Therefore, it is essential to know which critical value $\mathcal{A}_c$ separates the two regimes. In other words, we seek to determine a value of $\mathcal{A}_c$ such that the sequence α_j admits only one fixed point. This value is empirically found to be $\mathcal{A}_c = \mathrm{e}^{-1} \simeq 0.368$. As long as the attenuation is greater than e^{-1}, attenuation correction is accurate. With a starting value greater than 1, the sequence diverges.

Theorem: $\forall \mathcal{A} \in]0, 1[$, 1 is a fixed point of α_j.

If α^* is a fixed point of the α_j sequence, then we should have $\alpha^* = \mathcal{A}^{1-\alpha^*}$. Conversely we have

$$\mathcal{A} = \mathrm{e}^{\frac{\ln \alpha^*}{1-\alpha^*}}. \tag{19}$$

But in order to have only one fixed point for the α_n sequence, we must have $\alpha^* = 1$. Hence we deduce $\mathcal{A} = \mathrm{e}^{-1}$.

We can already note that n_e (and μ) can be correctly reconstructed over a large domain of the object. The critical value of the attenuation factor, i.e. $\mathcal{A}_c = 0.368$, lies precisely inside the range of $\mathcal{A}$-values found usually in practice, namely $0.99 < \mathcal{A} < 0.03$. Thus, there exists another domain of the object where the value of n_e is underestimated.

In SPECT imaging with ^{99m}Tc labeled radiotracers, the values of $\mathcal{A}$ are around $\mathcal{A} \sim 0.15$ (Zaidi and Hagasewa 2003). This is normal since we are considering photons which either barely skim the medium or traverse the medium, in which case they are strongly attenuated.

In conclusion, the region close to the point source is correctly reconstructed; however, n_e is underestimated in regions far away with increasing uncertainty as the distance from the point source increases. In other words, there is a 'critical distance' beyond which attenuation map reconstruction is not satisfactory.

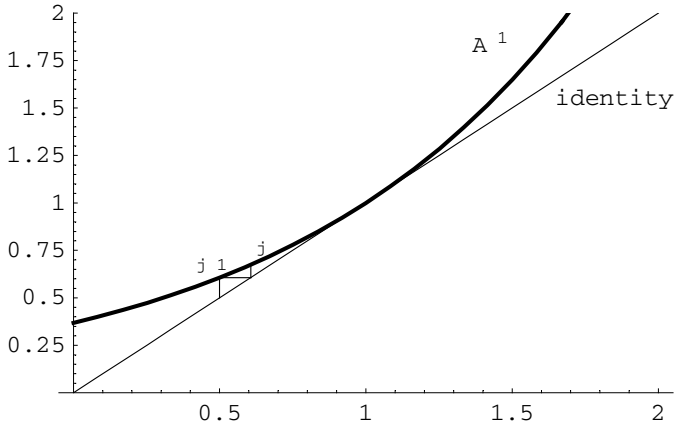

Figure 6. Critical value $\mathcal{A}_c = e^{-1}$: the sequence α_j has a second fixed point smaller than 1.

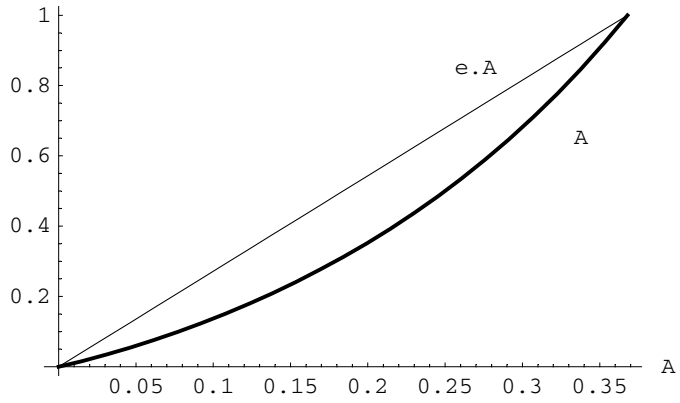

Figure 7. Plot of $\alpha^*(\mathcal{A})$ in the interval $0 < \alpha < e^{-1}$.

2.5.4. Additional correction when global photon attenuation is lower than $\mathcal{A}_c$. When attenuation is small, i.e. $\mathcal{A} < e^{-1}$, due to greater distances from the source, we can try to figure out how the error increases with the distance. Recall that an approximate value of the electronic density is related to its true value according to equation (17). The true error, after an infinite number of correction steps, is in fact the numerical factor α^* (limit of the sequence α_j, as $j \to \infty$). Therefore we should seek to express α^* in terms of $\mathcal{A}$ by inverting equation (19).

This inversion is readily expressed as

$$\alpha^*(\mathcal{A}) = \frac{\text{LambertW}(\mathcal{A} \ln \mathcal{A})}{\ln \mathcal{A}}, \tag{20}$$

where LambertW(x) is the solution of the equation $W\, e^W = x$. The behavior of $\alpha^*(\mathcal{A})$ is displayed in figure 7. Then an easy way to correct the data in this situation is just to multiply the results by $1/\alpha^*(\mathcal{A})$.

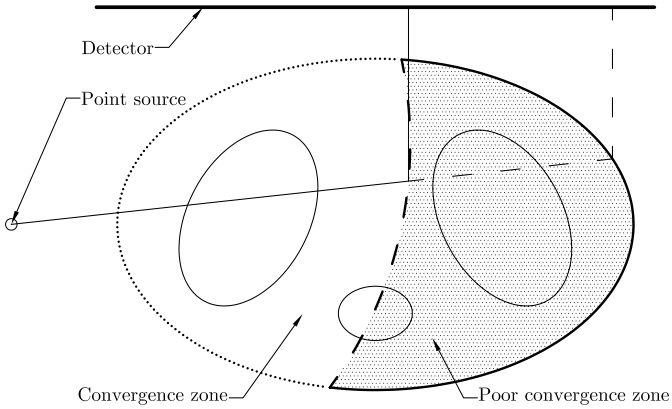

Figure 8. Convergence zone of the IAC algorithm.

Unfortunately $\mathcal{A}$ is not known and consequently we cannot perform the correction. One possible solution consists of determining α^* as a function of the distance traveled by the photon d. To this end, we shall make three observations (figure 8):

- First, we determine the convergence zone in which the ISDC algorithm produces good results. The border line is the bold dashed line shown on figure 8 along which $\alpha^* = \mathbf{1}$. This could be determined empirically while looking for scattering sites for which $\mathcal{A} = \mathrm{e}^{-1} = 0.368$. We will show later a better method to determine this line.
- We need to know the electronic density all around the poor convergence zone (shaded zone in figure 8). Knowing the real value of n_e at these points allows us to calculate the error α^* made with the IAC algorithm. Likewise, knowing the real value of n_e allows us to compute $\mathcal{A}$. Using prior knowledge (e.g. symmetry) about the object under study, n_e (and consequently attenuation) would be known at all points of the external frontier of the object. Alternatively the error could be also determined using a thin beam of photons skimming the object. Another solution is to place at the opposite site of the external emitting source a thin test object with known electronic density.
- Finally, we have to determine how $\mathcal{A}$ varies with distance in the poor convergence zone. We know that $\mathcal{A}(d)$ is of the form

$$\mathcal{A}(d) = \mathrm{e}^{-\sigma n_e d} = \mathrm{e}^{-d'}, \tag{21}$$

where $d' = \sigma n_e d$ and $d' > 1$ in the poor convergence zone. It is now possible to express α^* as a function of d':

$$\begin{aligned} \alpha^*(d') &= \frac{\mathrm{LambertW}(\mathcal{A}(d')\ln\mathcal{A}(d'))}{\ln\mathcal{A}(d')}. \\ &= \frac{\mathrm{LambertW}(-d'\mathrm{e}^{-d'})}{-d'}. \end{aligned} \tag{22}$$

Figure 9 shows the behavior of $\alpha^*(d')$. From the three previous observations and the expression of $\alpha^*(d')$, we are able to correct the n_e values in the poor IAC algorithm convergence zone.

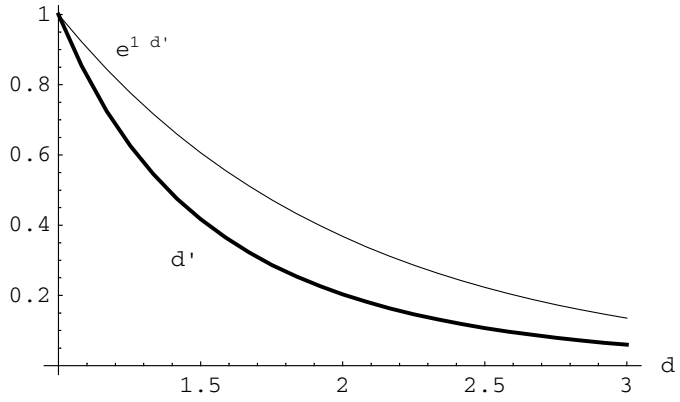

Figure 9. n_e error estimation using the IAC algorithm convergence. $\alpha^*(d')$ is given for $d' > 1$. For comparison, the function $e^{1-d'}$ is also depicted.

On both ends of the dashed segment in figure 8, α^* is known, and knowing the form of $\alpha^*(d')$, we know α^* everywhere.

2.5.5. Determination of the actual IAC algorithm zone convergence. The convergence zone of the corrections to n_e is the same as the zone where photon attenuation verifies $A > e^{-1}$. This could be empirically determined from the IAC algorithm results, but we propose here a better solution. Since $A = e^{-\sigma n_e d}$, we wish to have $-\sigma n_e d > -1$. Thus the limiting distance d_{lim} for the convergence of the IAC algorithm is given by

$$d_{\text{lim}} < \frac{1}{\sigma n_e}. \tag{23}$$

Providing that some prior information is available on the medium, a good approximation of d_{lim} could be obtained. Note that d_{lim} depends on σ, the cross section of the medium under study, which depends also on the incident photon energy. With higher energy photons, the IAC algorithm's good convergence zone could be enlarged.

In practice, we use the IAC algorithm for a medium in which n_e is constant over non-intersecting blocks. It is possible to improve further the convergence by working with appropriate parameters inside each block.

2.6. Phantom simulations

We have chosen a phantom representing a thoracic cage in order to simulate features occurring in typical SPECT imaging studies, i.e., a non-homogenous object consisting of three different biological tissues (lungs, soft tissue and bone).

The object schematically representing a human thorax is made up of three types of materials: bone (white), soft tissue (gray) and lungs (black). A cross section with ribs and spinal column, lungs and tissue is presented in figure 10.

We adopt the following values of linear attenuation coefficients at 140 keV photon energy: 0.28 cm^{-1} for bone, 0.15 cm^{-1} for water (soft tissues), 0.000 17 cm^{-1} for air and 0.042 cm^{-1} for lungs. Typical values of electron density are: 5.91×10^{23} cm^{-3} for bone, 3.34×10^{23} cm^{-3} for water, 3.61×10^{20} cm^{-3} for air and 0.634×10^{23} cm^{-3} (inhale) or 1.632×10^{23} cm^{-3} (exhale) for lungs.

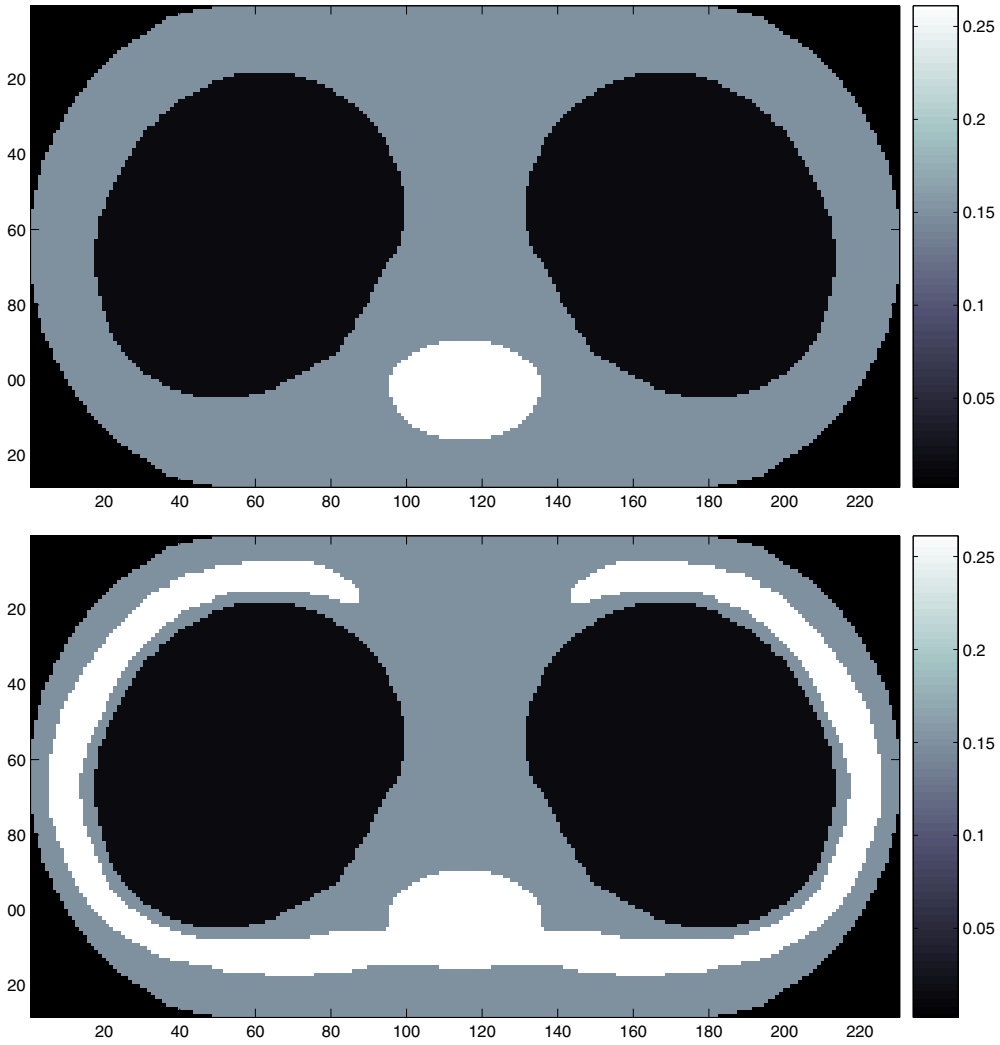

Figure 10. Representative slices of the original attenuation map of the object without ribs (top) and with ribs (bottom).

Table 1. Physical characteristics of some materials at 140 keV.

Material	n_e (cm^{-3})	Density (g cm^{-3})	μ/ρ (cm^2 g^{-1})
Bone	5.91×10^{23}	1.85	0.143
Water	3.34×10^{23}	1.00	0.150
Air	3.61×10^{20}	1.2×10^{-3}	0.139
Lung	see above	0.3	0.139

In table 1, physical characteristic values for bone, water, air and lungs are given.

The gamma camera is placed above the voxel-based phantom at a distance of 80 mm. The source, as shown in figure 1, is placed at 20 mm nearby the volume under study on its side.

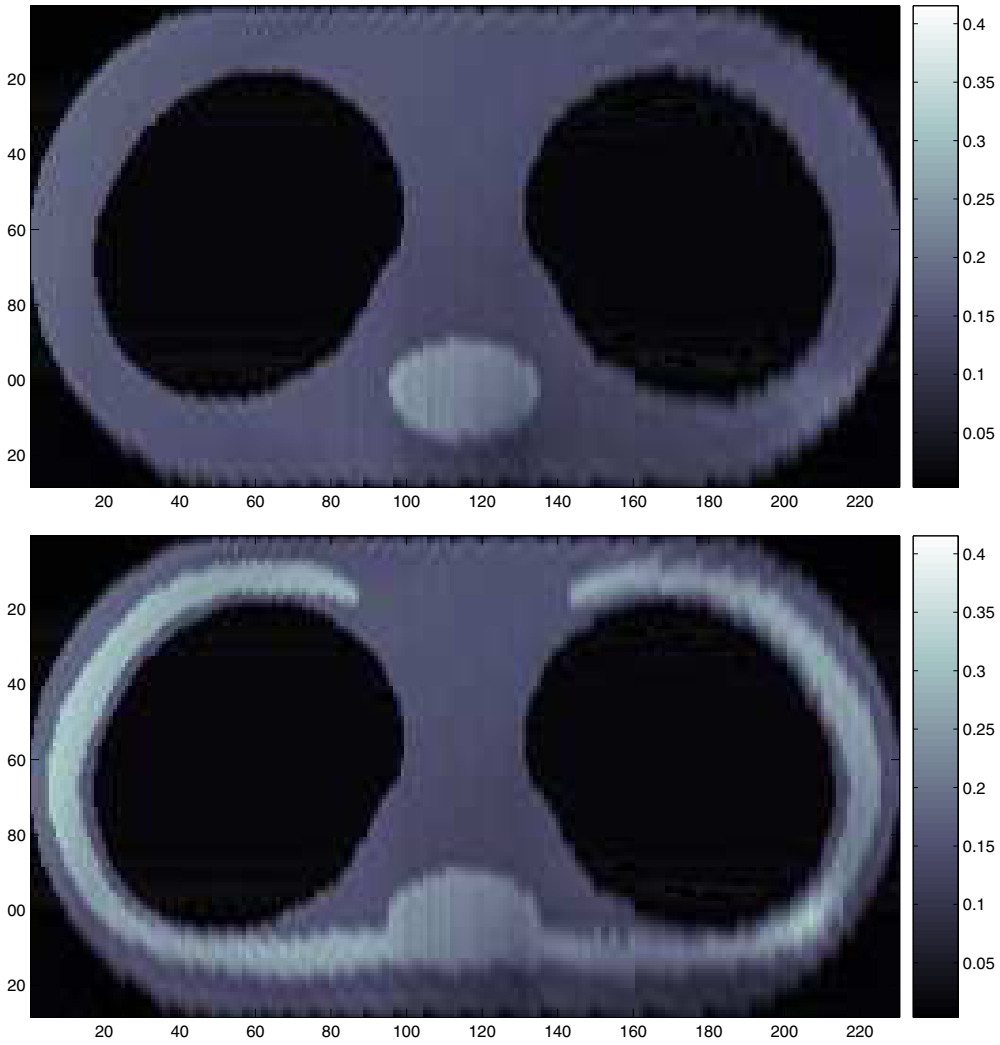

Figure 11. Representative slices of the reconstructed attenuation map corresponding to those shown in figure 10.

3. Results and discussion

Here we present the results of the reconstruction of the medium electron density (and attenuation μ) map from collected transmission data with the gamma camera operating in list mode. The detected photons are emitted by the external source and scattered (and attenuated) in the medium. The reconstruction method presented in section 2.1.1 and the IAC correction algorithm presented in section 2.2 were performed.

Figure 11 shows two representative slices of the 3D reconstructed transmission images. It can be seen that the left parts are more accurately recovered by the reconstruction procedure. This was expected since in our simulations, the transmission point source was on this side of the phantom (the gamma camera was placed above the medium, i.e. far from the spinal column).

The mean relative error (MRE_μ) between the original object, represented by (μ) and the reconstructed object represented by (μ^*), was used as a quantitative measure of image quality:

$$MRE_\mu = \frac{1}{N}\sum_{\ell}\frac{|\mu^*(\ell)-\mu(\ell)|}{|\mu(\ell)|}, \tag{24}$$

where N is the number of voxels of the voxel-based phantom and ℓ the voxel label. It was demonstrated that a good performance can be achieved after only eight iterations ($MRE_\mu = 17.92\%$). The second figure of merit used is the mean relative quadratic error ($MRQE_\mu$) between the original and the reconstructed object, which is defined by

$$MRQE_\mu = \frac{1}{N}\sum_{\ell}\left(\frac{\mu^*(\ell)-\mu(\ell)}{\mu(\ell)}\right)^2. \tag{25}$$

It was also shown that after eight iterations, a good performance can be reached with $MRQE_\mu = 16.82\%$.

4. Conclusion

The method presented in this paper to estimate the attenuation map via the electron density of a medium by measuring Compton scattered radiation from an appropriately placed external source has brought up convincing preliminary results of its working principle. The proposed attenuation correction method used with a conventional SPECT gamma camera allows us to obtain simultaneously two unknown functions: the attenuation map (via the electronic distribution) and the activity distribution from one set of measurements. It should be emphasized that this concept is based on Compton scattered radiation measurements, which is the original aspect stressed in this work. Several perspectives can be opened from here. This work may suggest the possibility of proposing a new scattered radiation-based emission/transmission imaging system having many advantageous properties: use of the same detector, same radionuclide, stationary acquisition for transmission scanning, etc. More importantly, what has been done for nuclear medicine imaging can be extended, in the same spirit, to other industrial applications such as non-destructive testing. Finally on the theoretical level, a tantalizing challenge to be tackled is naturally the analytic inversion of the attenuated compounded conical Radon transform (a-CCRT) as a natural extension of the attenuated x-ray transform (for which a solution was found only recently by Novikov (2002)). Such a solution would definitely confirm the imaging power of Compton scattered radiation proposed a few years ago (Nguyen and Truong 2002a).

Acknowledgments

This work was supported in part by the Swiss National Science Foundation under grant SNSF 3100A0-116547 and by grant ACI NIM TRC 2004 of the French Ministry of Research.

References

Barrett H H and Swindell W 1981 *Radiological Imaging I and II* (New York: Academic)

Battista J J and Bronskill M J 1981 Compton scatter imaging of transverse sections: an overall appraisal and evaluation for radiotherapy planning *Phys. Med. Biol.* **26** 81–99

Cesareo R, Hanson A L, Gigante G E, Prdraza L J and Mathaboally S Q G 1992 Interaction of keV photons with matter and new applications *Phys. Rep.* **213** 117–78

Clarke R L, Milne E N C and Van Dyk G 1976 The use of Compton scattered gamma rays for tomography *Invest. Radiol.* **11** 225–35

Gagnon D, Zeng G L, Links J M, Griesmer J J and Valentino F C 2001 Design considerations for a new solid state gamma camera: SOLSTICE *Proc. IEEE Nuclear Science Symp. and Medical Imaging Conf. (San Diego, Oct.)* vol 2, pp 1156–60

Gourion D, Noll D, Gantet P, Celler A and Esquerre J P 2002 Attenuation correction using SPECT emission data only *IEEE Trans. Nucl. Sci.* **5** 2172–9

Gullberg G T *et al* 1985 An attenuated projector-backprojector for iterative SPECT reconstruction *Phys. Med. Biol.* **30** 799–816

Hirasawa M and Tomitani T 2004 Effect of compensation for scattering angular uncertainty in analytical Compton camera reconstruction *Phys. Med. Biol.* **49** 2083–93

Holt R S, Cooper M J and Jackson D F 1984 Gamma-ray techniques for non destructive testing and imaging *Nucl. Instrum. Methods* A **221** 98–104

Hussein E M A 1989 Radiation scattering methods for non destructive testing and imaging *Int. Adv. Nondestr. Test.* **14** 301–21

Keidar Z, Israel O and Krausz Y 2003 SPECT/CT in tumor imaging? Technical aspects and clinical applications *Semin. Nucl. Med.* **33** 205–18

Kim H, Furenlid L R, Crawford M J and Barber H B 2006 SemiSPECT: a small-animal single photon emission computed tomography (SPECT) imager based on eight cadmium zinc telluride (CZT) detector arrays *Med. Phys.* **33** 465–74

King M A, Tsui B M, Pan T S, Glick S J and Soares E J 1996 Attenuation compensation for cardiac single-photon emission computed tomographic imaging: 2. Attenuation compensation algorithms *J. Nucl. Cardiol.* **3** 55–64

Kojima A, Matsumoto M, Takahashi M and Uehara S 1993 Effect of energy resolution on scatter fraction in scintigraphic imaging: Monte Carlo study *Med. Phys.* **20** 1107–13

Milhailescu L, Vetter K M, Burks M T, Hull E L and Craig W W 2007 SPEIR: A Ge Compton camera *Nucl. Instrum. Methods Phys. Res.* A **570** 89–100

Nguyen M K, Faye C, Eglin L and Truong T T 2001 Apparent images formation by Compton-scattered photons in Gamma-ray imaging *IEEE Signal Process. Lett.* **8** 248–51

Nguyen M K and Truong T T 2002a On an integral transform and its inverse in nuclear imaging *Inverse Problems* **18** 265–77

Nguyen M K and Truong T T 2002b Exact inversion of a compound conical Radon transform and a novel nuclear imaging principle *C. R. Acad. Sci. Paris* I **335** 213–7

Nguyen M K, Truong T T, Bui H D and Delarbre J L 2004 A novel inverse problem in γ-rays emission imaging *Inverse Problems Sci. Eng.* **12** 225–46

Norton S J 1994 Compton scattering tomography *J. Appl. Phys.* **76** 2007–15

Novikov R G 2002 An inversion formula for the attenuated x-ray transform *Ark. Math.* **40** 145–67

Radon J 1917 Über die bestimmung von funktionnen durch ihre integralwerte längs gewisser mannigfaltikeiten *Ber. Verh. Sachs. Akad. Wiss. Leipzig-Math.-Natur. Kl.* **69** 262–77

Truong T T, Nguyen M K and Zaidi H 2007 The mathematical foundations of 3D Compton scatter emission imaging *Int. J. Biomed. Imaging* **2007** 92780

Zaidi H 1999 Relevance of accurate Monte Carlo modeling in nuclear imaging *Med. Phys.* **26** 574–608

Zaidi H and Hasegawa B 2003 Determination of the Attenuation map in emission tomography *J. Nucl. Med.* **44** 291–315

Zaidi H and Koral K F 2004 Scatter modelling and compensation in emission tomography *Eur. J. Nucl. Med. Mol. Imaging* **31** 761–82

Zeng G L *et al* 2002 Image reconstruction algorithm for a rotating slat collimator *Med. Phys.* **29** 1406–12